Proceedings of the ASME 2016 International Mechanical Engineering Congress and Exposition
IMECE2016
November 11-17, 2016, Phoenix, Arizona, USA

IMECE2016-65538

INTEGRATING FIRST-PRINCIPLE CALCULATION AND PHASE-FIELD SIMULATION FOR LITHIUM DENDRITIC GROWTH ON THE ANODE OF A LITHIUM-ION BATTERY

Lei Chen
Department of Mechanical Engineering, Mississippi State University,
Mississippi State, MS, 39762

ABSTRACT

Lithium (Li) dendrite formation compromises the reliability of Li-ion batteries, either because dendrite pieces lose electrical contractor or growing dendrite penetrates the separator and leads to internal short-circuiting. In this paper, a multi-scale computational approach integrating phase-field model and first-principles calculation is proposed to predict the Li dendrite formation at the anode/electrolyte interface of Li-ion batteries. The first-principles calculation is employed to atomically determine the interfacial energy, which is subsequently fed into the phase-field model at the micro-scale. 1D distribution of fields is first analyzed to validate the proposed model. An apparent 2D tree-type Li dendrite, widely observed in experiments during electrodeposition, is produced using the model. Finally, the 2D dendritic evolution under different electrochemical conditions specified by the applied current densities is discussed.

INTRODUCTION

The success of electric vehicles (EVs) requires a significant increase in the specific capacity of current Lithium (Li) -ion batteries (1, 2). Li metal is an ideal anode material for rechargeable batteries due to its extremely high theoretical specific capacity (3862 mAh/g) and the lowest negative electrochemical potential. Li-O_2 and Li-S batteries using Li-metal as an anode have attracted much attention for their significantly high capacity compared to a regular Li-ion battery (3, 4). However, lithium dendrite formation can lead to degradation and failure of batteries, either because dendrite pieces lose electrical contact with the rest of the Li electrode (typically during Li stripping on discharge) or growing dendrites penetrate the separator and lead to short circuits (5-7). Thus, a good understanding of the mechanism of Li dendrite formation and growth is critical to mitigate or eliminate Li dendrites.

The important role of lithium dendrites in Li-ion batteries has stimulated numerous efforts on simulating the dendritic formulation. The first attempt to model the electrochemical dendrite growth was made by Monroe and Newman (7). They presented a comprehensive mathematical model for temporal evolution of dendrite tip height and growth velocity in Li-polymer cells. Recently, Akolkar (8, 9) extended this model by incorporating a concentration-dependent diffusion coefficient, with application to liquid electrolytes. More recently, Aryanfar et al. (10) proposed a coarse-grained Monte Carlo calculation to uncover the Li-dendrite mechanism, by dealing explicitly with Li^+ migration in time-dependent non-uniform electric fields. However, they either failed to explicitly capture the temporal evolution of electrode-electrolyte interface, or did not provide the thermodynamic parameters inputs physically.

Phase-field method (PFM) has been applied to a vast range of phenomena in materials processes, e.g., solidification, solid-state phase transformation, recrystallization, and grain growth (11, 12). PFM is formulated based on the theory of irreversible thermodynamics, and is advantageous in addressing the time-dependent evolving morphologies process, which is hard to implement in traditional sharp-interface model. The early attempt along this line was made by Guyer et al. (13, 14) who developed a 1D PFM to investigate the equilibrium state and kinetic behavior of electrochemistry. Later, Okajima et al. (15) simulated the 2D electrodeposition process by linking a Cahn-Hilliard equation with a Butler-Volmer type equation. Recently, Liang et al. (16) proposed a 1D formulation that captures the Butler-Volmer kinetics of electrodeposition. More recently Ely et al. (17) conducted a PFM study on the kinetics of Li electrodeposits by extending the asymptotic analysis of the phase field theory. However, all these models are assuming a linear electrochemical reaction kinetics that breaks down when the system is highly out of equilibrium (16, 18), e.g., under high charging voltage, or do not capture an apparent dendritic growth of electrodeposits. Therefore, in order to be more consistent with the nonlinear electrochemical kinetics, it is necessary to develop a PFM that is able to capture the nonlinear nature of the electrochemical reaction at the electrode-electrolyte interface.

In addition, the validity of the phase-field, to a large extent, relies on having accurate thermodynamic, mechanical and kinetic parameters. The first-principles calculation based on density function theorem (DFT) has been demonstrated to be a powerful tool to determine these necessary parameters based on properly constructed atomic structures, particularly those can hardly be measured by state-of-art experimental techniques. One of the key parameters is the Li metal/electrolyte interfacial energy and its anisotropy. However, the Li metal anode cannot be in direct contact with electrolyte in real batteries. Instead, Li metal is covered by a thin passivation layer called solid electrolyte interphase (SEI) (19), which is either artificially coated or naturally formed arising from a complex of electrolyte reduction reactions (20). Therefore, the development of a real experimental-driven Li metal/SEI interfacial structure of first-principles calculation is highly critical to obtain the accurate interfacial energy and its anisotropy.

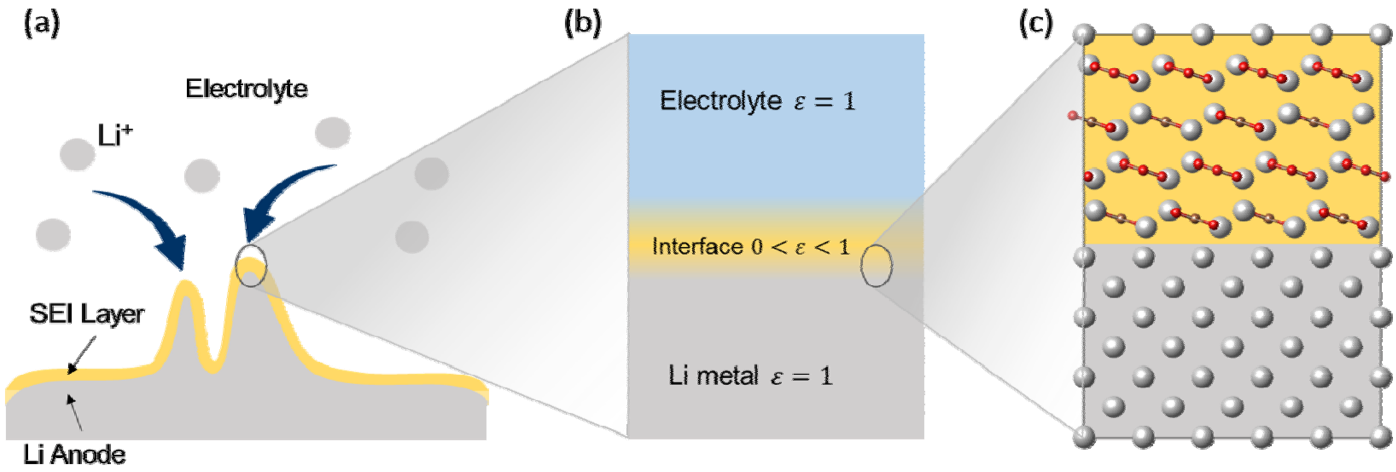

Figure 1 Schematic diagram of multi-scale study method: (a) Li dendrite growth mechanism, (b) phase-field model of the simulated system, the electrode $(\xi = 1)$ and electrolyte $(\xi = 0)$, (c) atomic scale SEI/Li interfacial model.

In this paper, a multi-scale framework, based on the combination of first-principles calculation and our recently developed PFM, is therefore proposed to predict the Li dendrite growth at electrode-electrolyte interface, as shown in Figure 1 (16). First-principles calculation, using the Li metal/SEI interfacial structure discussed above, is employed to calculate the interfacial energy and anisotropy as the important input for PFM. In the PFM, a nonlinear relationship is used to describe the electrode-electrolyte interface evolution and the thermodynamics driving force involving overpotential and ion concentration. The model automatically reproduces the Butler-Volmer type electrochemical kinetics at the moving diffuse-interface. The SEI layer is not explicitly included as an individual phase in this PFM. Further, a modified Poisson-Nernst-Planck (PNP) equation is included to solve ionic transport and local overpotential variation. The atomically determined interfacial energy and its anisotropy are incorporated into the phase field model, rendering it atomically informed and faithful in simulating the dendritic growth. The present multi-scale model is generally applicable to any non-equilibrium electrodeposition system exhibiting the dendritic growth.

FIRST PRINCIPLE CALCULATION

To calculate the interfacial energy and its anisotropy, Li metal/SEI interfacial supercells with incoherent sharp interfaces are carefully constructed based on interfacial orientations and in-plane misfit minimization. Due to that fact that LiF and Li_2CO_3 are two major components in both naturally formed and artificially coated SEI layers, the corresponding two interfaces, Li/LiF and Li/Li_2CO_3 are specifically used as the examples in this paper.

All first principle calculations are performed by Vienna Ab Initio Simulation Package (VASP) (22, 23) with plane wave basis sets and projected-augmented wave (PAW) pseudopotentials (24). The exchange-correlation (X-C) functional applied in the model is a generalized gradient approximation (GGA) of Perdew-Burke-Ernzerhof sol (PBEsol). Valence electron configurations for each element are as follows: $1s^2 2s^1$ for Li, $2s^2 2p^2$ for C, $2s^2 2p^4$ for O, and $2s^2 2p^5$ for F. The plane wave cutoff energy is tested to be 500 eV, and applied for all supercells. Prior to interface study, bulk and surface calculation were conducted for the validation purpose. For surface structures relaxation, one k-point was set in surface normal direction while in-plane k-points numbers remained the same as bulk calculation. The total energy of all structures were converged to 10^{-4} eV/supercell. Methfessel-Paxton smearing (order equals 1) was used for Li metal and Gaussian smearing was used for Li_2CO_3 and LiF, with a 0.2 eV energy broadening in all cases.

The surface energy from slab method is the difference between the total energy of the relaxed slab structure and the bulk energy with the same number of atoms. The thickness of slab and vacuum layer is assumed to be large enough to neglect the interaction between the two surfaces of the slab (At least 10 Å vacuum layer is tested and added between slab surfaces in this calculation). The surface energy can be expressed as

$$\gamma = \lim_{N\to\infty} \frac{1}{2S}\left(E_{Slab}^{N} - N \times E_{Bulk}\right) \tag{1}$$

where E_{Slab}^{N} is the total energy of the relaxed slab containing N units, E_{Bulk} is the unit bulk total energy, S is the surface area, and the coefficient 2 indicates two equivalent surfaces in the supercell. To avoid error caused by E_{Bulk} calculation with different supercells and different k-point mesh from E_{Slab}^{N}, Fiorentini and Methfessel method (25) was applied to obtain E_{Bulk} by linear fitting the slab supercell total energy data versus N and taking the slope of the straight line to reach the converged surface energy values efficiently with least atomic number of layers.

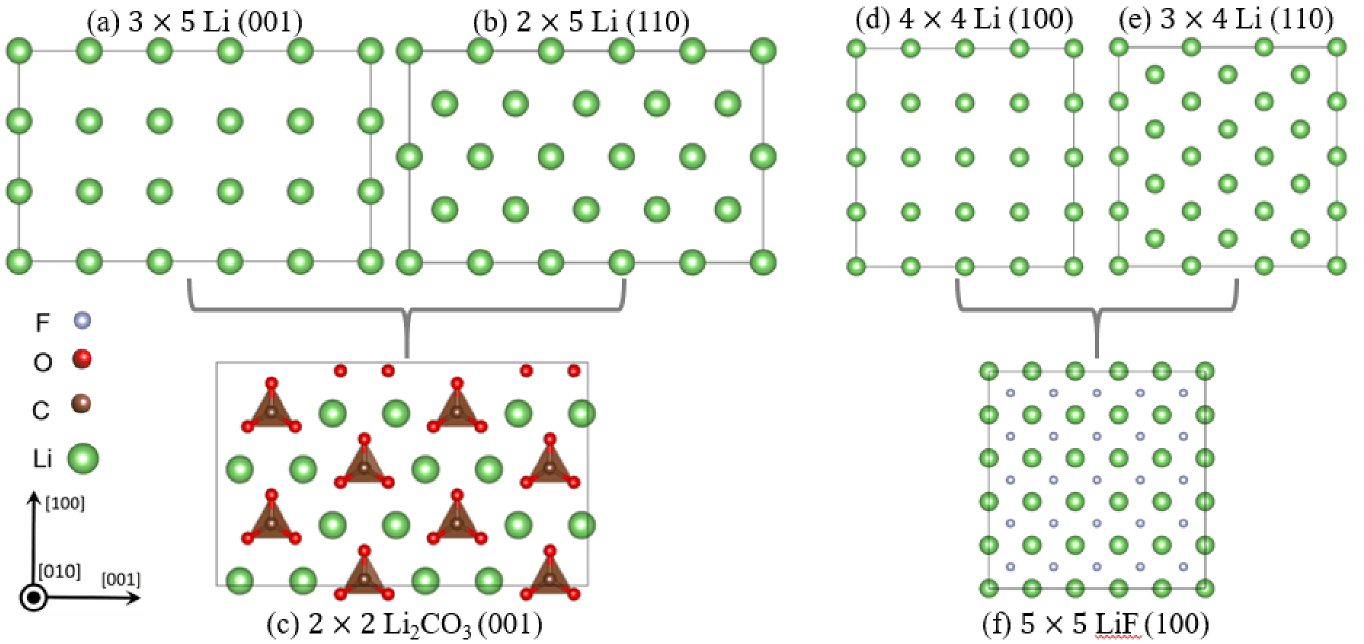

Figure 2 Top view of Interface structure with extended supercells.

Interface structures with extended supercells are then built and their initial as-constructed atomic structures are shown in Figure 2. Since Li is rather isotropic, the two lowest energy surfaces, (100) and (110), are both considered in the interface model. On the other hand, LiF and Li_2CO_3 are rather anisotropic, only the orientations with the lowest surface energy were considered. The supper lattice size of Li metal are selected to match the lowest energy surfaces, (100) of LiF and (001) of Li_2CO_3, respectively. Each surface was cleaved and expanded to match the counterpart, reducing the interfacial mismatches to ~3% for all interface supercells..

To obtain the stress-free interfacial energy, the following method (26) was applied on an interfacial supercell of constituents A and B. First, the constructed interface structures were fully relaxed (with respect to cell volume, shape and atomic coordinates) to their external stress-free states. Then, pure A and B bulk structures with the same interfacial geometry and similar atomic layer numbers, were relaxed along interface normal direction (z) respectively, with fixed strained in-plane (x and y) lattice vectors obtained from the fully relaxed interfacial geometry. Same k-point mesh and cut-off energy were used for the two steps. The interfacial energy can be then calculated by

$$\sigma = \frac{E_{AB(xyz)} - N_A E_{A(z)} - N_B E_{B(z)}}{2S} \tag{2}$$

where $E_{AB(xyz)}$ is the fully-relaxed total energy of the interfacial structure. $E_{A(z)}$ and $E_{B(z)}$ are the energies per atomic layer of the pure A and B bulk structures after constrained relaxation along interface normal direction (z direction) with fixed x and y lattice vectors. N_A and N_B are the atomic layer numbers of A and B in the interfacial supercell, respectively. S is the interfacial area and the factor 2 in front of S is due to the two interfaces in one interfacial supercell.

PHASE-FIELD MDOEL

A schematic representation of the model geometry in half cell of Li-ion batteries is shown in Figure 1(b). The model consists of a lithium metal surface in contact with a liquid electrolyte containing cation (Li^+) and anion (PF_6^-) species. When the batteries operates a high current densities or high-voltages, in addition to Li intercalation, Li^+ cation in a binary dilute electrolyte LiPF_6 transports through the SEI layer, and reacts with electrons e^- reduced to Li-atom at the surface of the electrode. This process can be illustrated by $\mathrm{Li}^+ + \mathrm{e}^- \rightarrow \mathrm{Li}$. The Gibbs free energy of the electrochemical system can be expressed by

$$G = \int_V \left[f_{ch}(c) + f_{grad}(\nabla c) + f_{elec}(c,\phi) \right] \mathrm{d}V \,, \tag{3}$$

where $c = \{c_a, c_+, c_-\}$ is the set of concentrations for Li-atom, Li^+ cation and PF_6^- anion respectively. A set of dimensionless concentrations is introduced in the form of $\{c_a = c_a / c_s,\ c_+ = c_+ / c_0,\ c_- = c_- / c_0\}$, where c_s is the site density of Li-metal and c_0 the standard bulk concentration of electrolyte solution. Note that the same symbols are used for each dimensionless concentration for convenience.

$f_{ch}(c)$ corresponds to the Helmholtz free energy density that is related to and the electrochemical potential, for which the expressions for different components in the electrodeposition reaction can be written as

$$\mu_{\mathrm{Li}^+} = RT \ln a_{\mathrm{Li}^+} + \mu_{\mathrm{Li}^+}^{\ominus} + F\phi_s \,, \tag{4}$$

$$\mu_e = RT \ln a_e + \mu_e^{\ominus} - F\phi_e \,, \tag{5}$$

$$\mu_{\mathrm{Li}} = RT \ln a_{\mathrm{Li}} + \mu_{\mathrm{Li}}^{\ominus} \,, \tag{6}$$

where ϕ_s and ϕ_e are, respectively, the electrostatic potential in the electrolyte solution and the electrode. The electrode-electrolyte interfacial potential difference is $\Delta\phi = \phi_e - \phi_s$. *RT* is the product of the molar gas constant, *R*, and the temperature, *T*. *F* is the Faraday's constant. a_i are the activity of component *i* (which could be Li^+ cation, or electrons e^-, or Li-atom). $\mu_i^{\ominus}$ denotes the reference chemical potential of species *i*.

In order to describe the diffuse interface in the present phase-field model, a continuous phase-field variable, ξ, with a physical correspondence to the dimensionless concentration of Li-atom, as $\xi = c_a$, is introduced. An arbitrary double well function $g(\xi) = W\xi^2(1-\xi)^2$ is used to describe the two equilibrium states for the electrode ($c_a = 1$) and the electrolyte ($c_a = 0$). *W/16* represents the barrier height. Thus, $f_{ch}(c)$ reads

$$f_{ch} = W\xi^2(1-\xi)^2 + c_0 RT\left(c_+ \ln c_+ + c_- \ln c_-\right) + \sum_i c_i \mu_i^{\ominus} \tag{7}$$

In addition, $f_{grad} = 1/2 \nabla c \cdot \kappa \nabla c$ is the gradient energy density associated with interfacial energy. The interfacial energy anisotropy, i.e., its dependence on the orientation of the electrode-electrolyte interface, is introduced in the system by expanding the gradient coefficient as $\kappa(\theta) = \kappa_0\left[1 + \delta\cos(\omega\theta)\right]$, where δ and ω are the strength and mode of the anisotropy, κ_0 is related to the surface energy γ, θ is the angle between the normal vector of interface and the reference axis.

$f_{elec} = \rho_e \phi$ is the electrostatic energy density where ϕ is the electrostatic potential, and ρ_e is the charge density that is expressed as $\rho_e = F\sum_i z_i c_i$, which involves the concentrations of all the species in the system.

Having these definitions, the electrochemical reaction rate, R_e, takes the variational form of

$$R_e = -k_0 a_+^{1-\alpha} a_{\mathrm{Li}}^{\alpha} \left\{ \exp\left[\frac{(1-\alpha)nF\eta}{RT}\right] - \exp\left[\frac{-\alpha nF\eta}{RT}\right] \right\} \tag{8}$$

where k_0 is the reaction rate constant. The anodic and cathodic charge-transfer coefficients α_a and α_c satisfy $\alpha_a = 1-\alpha$ and $\alpha_c = \alpha$ with asymmetry factor $0 < \alpha < 1$. In addition, the overpotential, η, is defined as

$$\eta = \Delta\phi - \Delta\phi^{eq} = \frac{\Delta\mu}{nF} = \frac{1}{nF}\sum_i \frac{\delta G}{\delta c_i} \tag{9}$$

This total overpotential is further defined as the sum of the activation overpotential η_a and the concentration overpotential η_c

$$\eta = \eta_a + \eta_c \tag{10}$$

with

$$.\ \eta_c = -\frac{RT}{nF}\ln\frac{a_{\mathrm{Li}^+} a^-}{a_{\mathrm{Li}}} \tag{11}$$

and

$$\eta_a = \Delta\phi - E^{\ominus} \,. \tag{12}$$

where

$$E^{\ominus} = \frac{\mu_{M^{n+}}^{\ominus} + n\mu_e^{\ominus} - \mu_M^{\ominus}}{nF} \tag{13}$$

is the standard half-cell potential. Assuming a dilute electrolyte solution in the system with $a_{\mathrm{Li}^+} = c_+$, and the electrons are always supplied on the surface of the electrode $a_e = 1$. In addition, the activity for Li-atom, a_{Li}, is expressed by

$$c_s RT \ln a_{\mathrm{Li}} = g'(c) - \kappa\nabla^2 c = g'(\xi) - \kappa\nabla^2\xi \tag{14}$$

based on the definition of activity (18), e.g., for species i, which is given by

$$a_i = \exp\left(\frac{1}{RT}\frac{\partial f_{mix}}{\partial c_i}\right). \tag{15}$$

where $f_{mix} = f_{ch} + f_{grad} - \sum_i c_i \mu_i^{\ominus}$ is the mixing free energy density relative to the standard state.

In the present model, we consider the phase-field evolves by the electrochemical reaction, R_e, thus

$$\frac{\partial\xi}{\partial t}=-k_0c_+^{1-\alpha}a_M^{\alpha}\left\{\exp\left[\frac{(1-\alpha)nF\eta}{RT}\right]-\exp\left[\frac{-\alpha nF\eta}{RT}\right]\right\}. \qquad (16)$$

after substituting the activities.

Considering the electrodeposition system physically, the driving force is generally contributed by two parts: interfacial free energy and the electrode reaction affinity. When the system is far from equilibrium, the driving force from interfacial energy or curvature variation is usually small relative to the electrode reaction. Therefore, the temporal evolution of phase-field is considered linearly proportional to the interfacial free energy and exponentially to the thermodynamics driving force related electrode reaction, that is

$$\begin{aligned}\frac{\partial\xi}{\partial t}&=-L_\sigma\left(g'(\xi)-\kappa\nabla^2\xi\right)\\&-L_\eta h'(\xi)\left\{\exp\left[\frac{(1-\alpha)nF\eta_a}{RT}\right]-\tilde{c}_+\exp\left[\frac{-\alpha nF\eta_a}{RT}\right]\right\}\end{aligned} \qquad (17)$$

where $h(\xi)=\xi^3\left(6\xi^2-15\xi+10\right)$ is an interpolating function, $\eta_a=\Delta\phi-E^\ominus$ is the activation overpotential, and $E^\ominus$ is the standard half-cell potential. L_σ and L_η are, respectively, the interface mobility and the reaction-related constant.

For the species diffusion in the electrodepostion system, the flux of species i is proportional to the thermodynamic driving force in the form of

$$J_i=-M_ic_i\nabla\mu_i=-D_i\left(\nabla c_i+c_i\nabla\frac{F\phi}{RT}\right), \qquad (18)$$

In the model, Li-atom is regarded as immobile without diffusion process, while the electrochemical reaction provides a source term for the evolution of Li^+ cation. Ignoring the effect of PF_6^- anion transport, the diffusion of Li-atom is governed by

$$\frac{\partial c}{\partial t}=c_sR_e\left(\frac{nF\eta}{RT}\right)\ or\ \frac{\partial\tilde{c}}{\partial t}=R_e\left(\frac{nF\eta}{RT}\right). \qquad (19)$$

The Li^+ cation diffuses following

$$\frac{\partial c_+}{\partial t}=\nabla\cdot\left[D^{eff}\nabla c_++\frac{D^{eff}c_+}{RT}nF\nabla\phi\right]-c_sR_e\left(\frac{nF\eta}{RT}\right). \qquad (20)$$

Combining Eqs. (19-20) yields

$$\frac{\partial\tilde{c}_+}{\partial t}=\nabla\cdot\left[D^{eff}\nabla\tilde{c}_++\frac{D^{eff}\tilde{c}_+}{RT}nF\nabla\phi\right]-\frac{c_s}{c_0}\frac{\partial\xi}{\partial t}, \qquad (21)$$

where the effective diffusion coefficient is interpolated by $D^{eff}=D^eh(\xi)+D^s\left(1-h(\xi)\right)$, where D^e and D^s are the Li^+ diffusion coefficients in the electrode (which is almost zero) and the SEI layer respectively. The first two terms duplicate the classical Nernst-Planck equation. The last term is to describe the accumulation/consuming of Li^+ cation due to the electrochemical reaction on the electrode surface.

For the electrostatic potential distribution, assuming the charge neutrality in the system, we consider the current density is conserved described by Poisson equation including a source term I_R to represent the charge that enters or leaves due to the electrochemical reaction, as

$$\nabla\cdot\left[\sigma^{eff}\nabla\left(\phi(r,t)\right)\right]=I_R\,, \qquad (22)$$

RESULSTS AND DISCUSSION

1. First Principle Calculation

The computed surface energy values of Li, Li_2CO_3 and LiF are first compared with the available experimental measurements and other computational results for the validation purpose. The excellent agreement is clearly observed, whatever the material orientations [30-34] as given in Table 1. It is also found the lowest surface energy is usually in the most close-packed directions with least number of daggling bonds. To be specific, for b.c.c. Li metal, the three low-indices surfaces, (100), (110) and (111), show close values of surface energies, with the lowest of 0.49 J/m^2 along (100) direction. For monoclinic Li_2CO_3, (001) orientation has the lowest surface energy of 0.18 J/m^2, prominently smaller than the other two low-indices surfaces, $(\bar{1}01)$ and (110). For rocksalt-structured LiF, the (100) orientation has the lowest surface energy of 0.36 J/m^2, almost two times smaller than (110) direction. The LiF (111) surface is not energetically favorable due to net dipole along surface normal direction produced by alternating stack of F-only and Li-only layers.

Table 1 Comparison of DFT calculated surface energies with the experimental references [30-34].

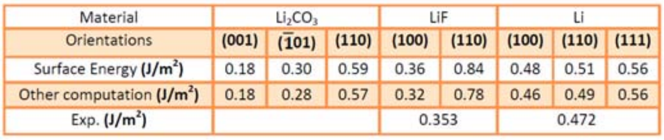

Material	Li_2CO_3			LiF		Li		
Orientations	**(001)**	**$(\bar{1}01)$**	**(110)**	**(100)**	**(110)**	**(100)**	**(110)**	**(111)**
Surface Energy **(J/m^2)**	0.18	0.30	0.59	0.36	0.84	0.48	0.51	0.56
Other computation **(J/m^2)**	0.18	0.28	0.57	0.32	0.78	0.46	0.49	0.56
Exp. **(J/m^2)**				0.353		0.472		

The energetic results for the four structures are then calculated and listed in Table 2. Compared with Li/LiF interfaces, the Li/Li_2CO_3 interfaces have substantially lower energies (~50%) in both Li (100) and (110) directions. The

Table 2 DFT-calculated energies for different representative interfaces in SEIs.

	Li(001)/Li_2CO_3 (001)	**Li(110)/Li_2CO_3 (001)**	**Li(001)/LiF (001)**	**Li(110)/LiF (001)**
Formation Energy (10^{-18} J/unit cell)	1.836	1.926	3.103	3.267
Interfacial Energy (J/m^2)	0.498	0.573	0.747	0.803
Work of Separation (J/m^2)	0.167	0.124	0.093	0.065
Strain Energy (MJ/m^3)	52.711	6.248	16.342	1.121

lower interfacial energy of Li_2CO_3/Li interface are closely related to the total energy decrease from larger lattice distortion after relaxation as shown in Figure 3, in which the final fully-relaxed four interfacial supercells are plotted. Compared with LiF/Li interfaces, the relaxed Li_2CO_3/Li interfaces underwent more drastic structural changes with large distortion in the CO_3 layer near the interfacial region. By contrast, the relaxed LiF/Li interfaces experienced less lattice distortion, and instead, only slight atomic layer bending near interfacial region is observed.

In respect to the Li (100) and (110) orientations, the former shows higher work of adhesion and lower interfacial energy values in contact with either LiF or Li_2CO_3. Since Li (110) and (100) have similar surface energy, the interfaces with Li(100) are more stable when they both exist and are covered by LiF or Li_2CO_3, while (110) surface may become exposed again due to delamination. One interesting finding is the difference between the interfacial energies of Li (100) and (110) interfaced with the same material, either LiF or Li_2CO_3, is prominently small (~10%), which is close to the Li metal surface anisotropic difference. Therefore, it is highly possible that the surface energy anisotropy of Li metal dominates the anisotropy of Li/SEI interface despite the complication in the structure of the multicomponent SEI.

2. Phase-field Results

We apply the present nonlinear phase-field model to a realistic, $\mathrm{Li}^+ + \mathrm{e}^- \rightarrow \mathrm{Li}$, electrodeposition system, where the electrode is composed of pure Li-metal, while the electrolyte solution. includes cation (Li^+) and anion (PF_6^-) species such reaction is a typical electrode reaction in half cell of Li-ion batteries and the corresponding parameters characterized from experimental studies or modelling references [16, 29, 30] are detailed in Table 3.

The phase-field model is simulated using a finite element method on the platform of COMSOL Multiphysics 5.2, under an adaptive grid. Only the protuberant is initially considered for the electrode in the model to reduce the computational cost, with the size of electrolyte solution set to $500 \times 500\ \mu\mathrm{m}$. On the mesh sensitive study, the system mesh size is set as 140×140 with a minimum grid spacing of $d_{\min} = 2\ \mu\mathrm{m}$. We use an implicit time integration, with a time step of $\Delta t = 0.2\ \mathrm{s}$. The Li^+ bulk concentration is employed as

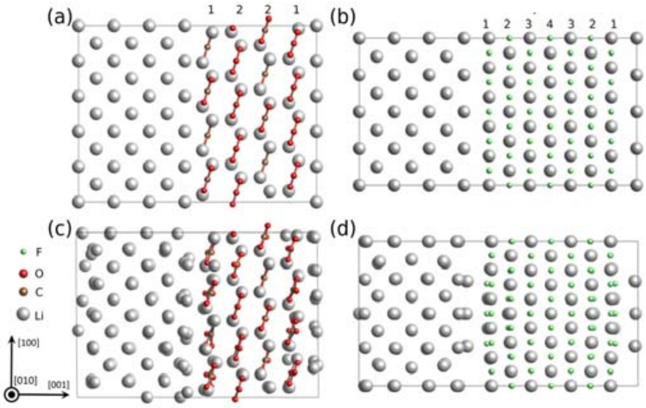

Figure 3 Atomistic study of the SEI components, from our preliminary first principles modeling. (a) As-constructed atomic structure and (b) fully-relaxed structure of a $Li(001)/Li_2CO_3(001)$ interface. (c & d) Same as (a & b), except for a Li(001)/LiF(001) interface.

Table3. Phase-field model parameters

	Real value		Normalized value	
Parameter	Symbol	Value	Symbol	Value
Interfacial mobility	L_σ	$2.5 \times 10^{-6}\ \mathrm{m}^3/(\mathrm{J} \times \mathrm{s})$	$\tilde{L}_\sigma = L_\sigma \times (E_0 \times \Delta t_0)$	2000
Reaction constant.	L_η	$1.0\ /\ \mathrm{s}$	$\tilde{L}_\eta = L_\eta \times \Delta t_0$	4000
Gradient energy coeff.	κ	$5 \times 10^{-5}\ \mathrm{J/m}$	$\tilde{\kappa} = \kappa / (E_0 \times l_0^{\ 2})$	0.01
Barrier height	W	$3.75 \times 10^5\ \mathrm{J/m}^3$	$\tilde{W} = W / E_0$	0.25
System size	l	500 µm	$\tilde{l} = l / l_0$	5.0
Time step	Δt	0.2 s	$\Delta\tilde{t} = \Delta t / \Delta t_0$	5×10^{-5}
Dif. coeff. in electrode	D^e	$7.5 \times 10^{-13}\ \mathrm{m}^2/\mathrm{s}$	$\tilde{D}^e = D^e / (l_0^{\ 2} / \Delta t_0)$	0.03
Dif. coeff. in solution	D^s	$7.5 \times 10^{-10}\ \mathrm{m}^2/\mathrm{s}$	$\tilde{D}^s = D^s / (l_0^{\ 2} / \Delta t_0)$	30
Con. in electrode	σ^e	$1.0 \times 10^7\ \mathrm{S/m}$	$\tilde{\sigma}^e = \sigma^e / (\frac{l_0^{\ 2}}{\Delta t_0} \cdot \frac{c_o F^2}{RT})$	10^9
Con. in solution	σ^s	1.0 S/m	$\tilde{\sigma}^s = \sigma^s / (\frac{l_0^{\ 2}}{\Delta t_0} \cdot \frac{c_o F^2}{RT})$	100

$c_0 = 1.0\times10^3\ \mathrm{mol/m^3}$. The site density of Li-metal is inverse of the volume of one mole Li-atom that is given by $c_s = 1/V = \rho_{\mathrm{Li}} / m_{\mathrm{Li}} = 7.64\times10^4\,\mathrm{mol/m^3}$, where m_{Li} and ρ_{Li} are molar mass and density of Li, respectively. All the parameters are normalized by a characteristic energy density $E_0 = 1.5\times10^6\,\mathrm{J/m^3}$, a characteristic length $l_0 = 100\ \mu\mathrm{m}$, and a characteristic time step $\Delta t_0 = 4000\ \mathrm{s}$. The symmetric factor $\alpha = 0.5$ is speculated in this work, unless otherwise specified.

Figure 4 shows the calculated 1D field distribution of phase-field, electric potential and Li^+ concentration. Both the potential and concentration fields have jumps at the electrode-electrolyte interface. The order parameter ξ equals 1 in the electrode and 0 in the electrolyte and has a diffuse interface. The Li^+ concentration in the vicinity of electrode increases away from the electrode surface due to charging condition. The total electric potential drop in this half-cell system includes three parts. The potential drop in the electrolyte is due to the ionic conduction, the potential drop across the interface because of the electrochemical reaction and Ohmic potential drop in the electrode where it is almost flat due to the high conductivity of lithium metal. The overpotential across the interface is taken as the thermodynamic driving force. The overpotential slightly increases with the time which corresponds to the increasing electrochemical reaction rate. During the electro-deposition process, Li^+ is transferred to Li metal due to the electrochemical reaction at the electrode/electrolyte interface, and the motion of the electrode/electrolyte interface characterizes the Li dendrite growth. Moreover, it is able to handle the complex microstructure evolution of Li dendrite growth in 2D space.

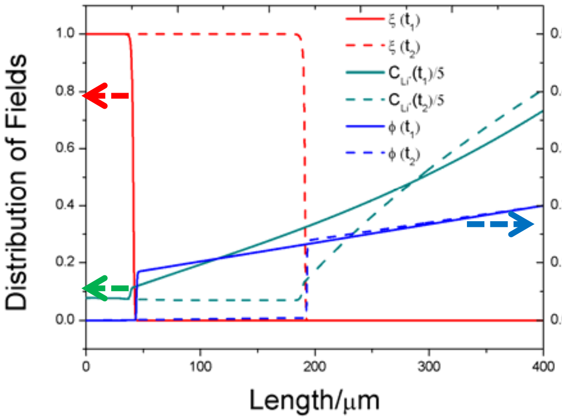

Figure 4 Distribution of order parameter, Li+ concentration and potenital in 1D.

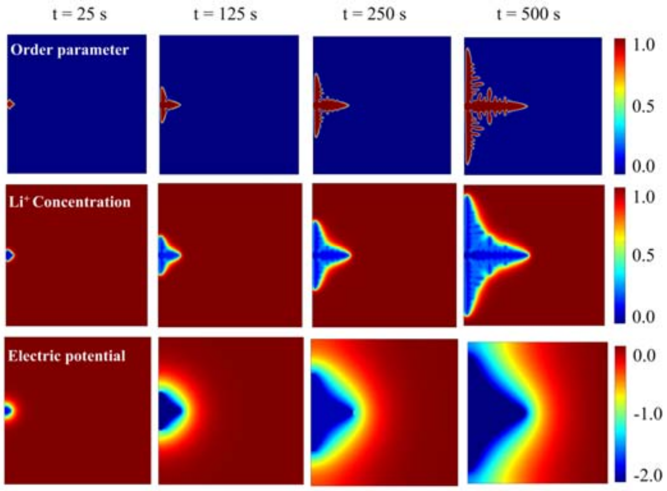

Figure 5 The 2D snapshots of order parameter ξ, Li^+ concentration $\tilde{c}$, and electric potential ϕ at various times.

2D simulations of lithium dendrite growth are then presented in which the anisotropic interfacial energy is fed into phase-field model. We start with a case where an artificial nucleation occurs at the center of electrode-electrolyte interface to illustrate the distributions of different fields Figure 5 shows the snapshots of the phase-field order parameter, Li^+ concentration and electric potential distributions as a function of evolution time by solving Eqs.(8-10). The local variations of Li^+ concentration and electric potential are both clearly seen. During the charging operation, the growth of phase-field (i.e., electrodeposit) can be related to the Li^+ concentration and electric potential by reaction kinetics in which surface tension (i.e., interfacial energy) also appears. This in turn results in a concentration gradient as well in an electric potential gradient at the neighborhood of the electrode and/or the deposit. The tips of deposits have larger concentration and electric potential gradients which give larger overpotential and force their faster growth. We should note that the overpotential, as a function of Li^+ concentration and electric potential, is taken as a field in our simulation which is different from the mathematical model that always taken as a single value. The overpotential across the interface is automatically taken as the thermodynamic driving force based on Eq.(8). The lithium deposition begins when the overpotential is less than zero.

In the real condition, charging conditions for a lithium ion battery can be divided as fixed charging current density type and fixed applied potential type. In this model, we supposed that the potential applied at the right side of this half-cell is constant and the left boundary condition is the Neumann boundary condition. The charging condition is the same as Newamn's model as $\nabla C_{Li^+} = -\dfrac{I(1-t_+^0)}{D_{Li^+}^L F}$. Figure 6 shows the dendritic morphologies under two charging current density

$2\ \mathrm{mA/cm^2}$ and $5\ \mathrm{mA/cm^2}$ at a certain time step. The deposit is unstable for all cases. The local inhomogeneities of deposits are expected to induce local variations of current density, hence of the concentration gradient. Because of the electrochemical reaction, the deposit grows with Li ions deposition. Simultaneously, part of Li ions can be deposited onto electrode surface to form the continuous dense lithium layer. However, the growth of dense layer is relatively slow compared with the growth of deposit due to the inhomogeneity of current densities. Clearly, the larger charging current density will increase the lithium ion concentration at the anode surface which gives the larger driving force, leading longer and thicker deposits.

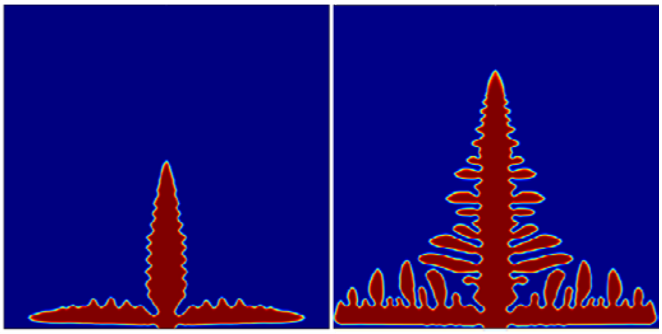

Figure 6 Diagram showing the effect of applied current density on dendritic patterns.

CONCLUSIONS

In summary, a multi-scale computational approach integrating phase-field model and first-principles calculation is proposed to predict the Li dendrite formation at the anode/electrolyte interface of Li-ion batteries. A thermodynamically consistent phase-field model, accounting for the nonlinear reaction kinetics, has been proposed to investigate the dendritic patterns, making use of the first-principles calculation that is employed to atomically determine the interfacial energy. Three different dendritic patterns have been discovered depending on the applied voltage and the interface morphology. A phase diagram was proposed, which could potentially be used as the guidance to experimentally control of Li-dendrite patterns. Analysis on the dendritic patterns demonstrates that the large applied voltage or the flat protuberant at the interface contributes to the side branches of dendrites, and even promotes an unstable tip-splitting.

ACKNOWLEDGMENTS

Lei Chen is grateful for the financial support by the Start-up funding from Mississippi State University. The computer simulations were carried out on the LION clusters at the Pennsylvania State University as well as the clusters of High Performance Computing Collaboratory (HPC²) at Mississippi State University.

REFERENCES

1. B. Scrosati and J. Garche, J. Power Sources, 195, 2419 (2010).
2. W. Xu, J. Wang, F. Ding, X. Chen, E. Nasybulin, Y. Zhang and J.-G. Zhang, Energy Environ. Sci (2014).
3. P. Andrei, J. P. Zheng, M. Hendrickson and E. J. Plichta, J. Electrochem. Soc, 159, A770 (2012).
4. M. S. Park, S. B. Ma, D. J. Lee, D. Im, S.-G. Doo and O. Yamamoto, Sci. Rep., 4 (2014).
5. Z. Li, J. Huang, B. Yann Liaw, V. Metzler and J. Zhang, J. Power Sources, 254, 168 (2014).
6. K. Nishikawa, T. Mori, T. Nishida, Y. Fukunaka and M. Rosso, J. Electroanal. Chem, 661, 84 (2011).
7. C. Monroe and J. Newman, Journal of The Electrochemical Society, 150, A1377 (2003).
8. R. Akolkar, Journal of Power Sources, 246, 84 (2014).
9. R. Akolkar, Journal of Power Sources, 232, 23 (2013).
10. A. Aryanfar, D. Brooks, B. V. Merinov, W. A. Goddard, A. J. Colussi and M. R. Hoffmann, The Journal of Physical Chemistry Letters (2014).
11. L. Chen, J. Chen, R. Lebensohn, Y. Ji, T. Heo, S. Bhattacharyya, K. Chang, S. Mathaudhu, Z. Liu and L. Chen, Computer Methods in Applied Mechanics and Engineering (2014).
12. L.-Q. Chen, Annual review of materials research, 32, 113 (2002).
13. J. E. Guyer, W. J. Boettinger, J. A. Warren and G. B. McFadden, Physical Review E, 69, 021603 (2004).
14. J. E. Guyer, W. J. Boettinger, J. A. Warren and G. B. McFadden, Physical Review E, 69, 021604 (2004).
15. Y. Shibuta, Y. Okajima and T. Suzuki, Science and Technology of Advanced Materials, 8, 511 (2007).
16. L. Liang, Y. Qi, F. Xue, S. Bhattacharya, S. J. Harris and L.-Q. Chen, Phys. Rev. E, 86, 051609 (2012).
17. D. R. Ely, A. Jana and R. E. García, Journal of Power Sources, 272, 581 (2014).
18. M. Z. Bazant, Accounts of chemical research, 46, 1144 (2013).
19. E. Peled, Journal of The Electrochemical Society, 126, 2047 (1979).
20. K. Leung, Chemical Physics Letters, 568, 1 (2013).
21. S. Shi, Y. Qi, H. Li and L. G. Hector Jr, The Journal of Physical Chemistry C, 117, 8579 (2013).
22. G. Kresse, Phys. Rev. B, 54, 11 (1996).
23. G. Kresse and J. Furthmüller, Physical Review B, 54, 11169 (1996).
24. G. Kresse and D. Joubert, Physical Review B, 59, 1758 (1999).
25. V. Fiorentini and M. Methfessel, Journal of Physics: Condensed Matter, 8, 6525 (1996).
26. Y. Wang, Z.-K. Liu, L.-Q. Chen and C. Wolverton, Acta Materialia, 55, 5934 (2007).
27. R. Kobayashi, Physica D: Nonlinear Phenomena, 63, 410 (1993).

28. G. B. McFadden, A. A. Wheeler, R. J. Braun, S. R. Coriell and R. F. Sekerka, Phys. Rev. E, 48, 2016 (1993).
29. A. A. Wheeler, B. T. Murray and R. J. Schaefer, Physica D, 66, 243 (1993).
30. M. Bruno and M. Prencipe, Surface science, 601, 3012 (2007).
31. S. P. Jand and P. Kaghazchi, Journal of Physics: Condensed Matter, 26, 262001 (2014).
32. K. Kokko, P. Salo, R. Laihia and K. Mansikka, Surface science, 348, 168 (1996).
33. W. Tyson and W. Miller, Surface Science, 62, 267 (1977).
34. J. J. Gilman, Journal of Applied Physics, 31, 2208 (1960).
35. L. O. Valøen and J. N. Reimers, J. Electrochem. Soc, 152, A882 (2005).